A statistical study of trans-equatorial loops from 2006 to 2020

Zihan Yu [1,2]★ Jie Chen,[1]★ Jihong Liu,[3]★ Alexei A. Pevtsov [4] Ziyao Hu,[1,5] Zhike Xue,[6] Jiangtao Su[1,5] and Yuanyong Deng[1,5]

[1]*National Astronomical Observatories, Chinese Academy of Sciences, Beijing 100101, China*
[2]*China School of Physics and Astronomy, China West Normal University, Nanchong 637000, China*
[3]*Shi Jiazhuang University, Shi Jiazhuang 050035, China*
[4]*National Solar Observatory, Boulder, CO 80303, USA*
[5]*China School of Astronomy and Space Science, University of Chinese Academy of Sciences, Beijing 100049, China*
[6]*China Yunnan Observatories, Chinese Academy of Sciences, Kunming 650216, China*

ABSTRACT

We studied trans-equatorial loops (TLs) statistically from December 2006 to 2020. During this period, 160 TLs were identified, and 12 per cent of all active regions are connected by TLs. The result shows that 74 per cent of TLs are connected to regions of preceding magnetic polarity (PTLs), and only 26 per cent of TLs are connected to regions of following magnetic polarity (FTLs). The dominance of PTLs is related to Joy's law. Moreover, the average length of TLs is 20°, and their lengths decrease during the solar cycle. By comparing the number of TLs and the smoothed monthly mean number of sunspots from 2009 to 2018, 88 per cent of the TLs appeared near the solar maximum (2014 ± 2). We noted that the closer a sunspot is to the equator, the easier it is for a TL to form. Furthermore, the tilt angle and latitudinal asymmetry of TL foot-points are independent of the solar cycle.

Key words: Sun: activity – Sun: atmosphere – Sun: corona – Sun: magnetic fields – Sun: photosphere.

1 INTRODUCTION

The trans-equatorial loop (TL) is a brilliant, large-scale loop structure that spans both hemispheres. Skylab data collected in the 1970s (Chase et al. 1976; Svestka et al. 1977) sparked interest in the TL. Furthermore, it is the first time the TL has been detected. The Yohkoh satellite was launched in 1991. A significant number of soft X-ray images of the Sun have been taken by Yohkoh Satellite's soft X-ray telescope (SXT) during the time of more than ten years and hundreds of TLs have been discovered. Later, the Hinode X-Ray Telescope (XRT) was developed as a successor of Yohkoh Soft X-Ray Telescope.

Using Skylab data, Chase et al. (1976) found that the average length of TLs, projected along the line of sight is 20°, with the longest being 37°. Later, Fárník, Karlický & Švestka (1999) reported two long TLs with lengths of 47 and 61 heliographic degrees, which is well above the limit assumed by Chase et al. (1976). Pevtsov (2000) performed a statistical study of the TLs by taking the data from Yohkoh/SXT. They found an average TL length of 30° and that the length varies during the different phases of the solar cycle.

It is generally believed that magnetic reconnection causes the formation of TL. By observing active regions (ARs) 12 472 and 12474, Svestka et al. (1977) concluded that magnetic reconnection of magnetic field lines extending to the equator in both ARs is at the origin of the TL. Tsuneta (1996) found an X-type TL, which is

a strong evidence that the TL is the result of an X-type magnetic reconnection. Pevtsov (2000) showed examples of TLs that fit the pattern of Y-type reconnection geometry. Recently, Ghosh & Tripathi (2020) reported on the formation and evolution of the TL from 10 to 14 December 2014 using observations obtained by imaging and spectroscopy, based on the analysis of temperature, density, velocity, and other physical properties in the X region. They concluded that the TLs were formed by magnetic reconnection and provided measurements of plasma parameters in X regions. Chen et al. (2020) proposed that two homologous TLs were formed by reconnection between magnetic field lines extending from ARs to the high corona, based on the evolution of related ARs and the generation of large TLs. Pevtsov (2004) studied the general properties of TLs and their agreement with the temperature-length scaling law. The temperature-length scaling law is defined as:

$$T_{\max} = 1.4 \times 10^3 (pL)^{(1/3)}, \tag{1}$$

where $T_{\max}$ is maximum temperature, p is the constant pressure, and L is the full length of the loop (Kano & Tsuneta 1995). He concluded that some trans-equatorial structures are magnetic separators and not magnetic loops. Magnetic separators mean they do not form loops. He also found that about 35 per cent of all ARs have trans-equatorial connections at some point in their development.

Large-scale TLs are also somewhat related to solar phenomena such as flares, coronal mass ejections (CME), and EIT waves. Khan & Hudson (2000) reported that shock waves generated by flares can destabilize TL, leading to the sudden disappearance of homologous TL. The disappearance of TL was closely linked to the CME. Delannée (2000) observed that CME can affect the magnetic

---

★ E-mail: 1847372937@qq.com (ZY); chenjie@bao.ac.cn (JC); 1102066@sjzc.edu.cn (JL)

field topology, leading to TL brightening, or dimming phenomena. She also proposed a scenario for how flares (TLs), CME, and EIT waves are related to each other. Balasubramaniam et al. (2005) observed a halo CME associated with the eruption of a large-scale TL. Before the disappearance of the TL, they observed the development of successive chromospheric brightenings propagating away from the origin of the eruption. This evolution was interpreted as evidence of sequential reconnection events when TL/CME were lifted from the solar corona. Long et al. (2017) found that a TL system exhibited a decaying oscillation due to the impact of an EIT wave observed on 2012 July 6, and they estimated the magnetic field strength of the loop system by examining the decaying oscillation of the loop system.

In most models of the solar dynamo, there are two key processes: the generation of the toroidal magnetic field by winding up the poloidal field through differential rotation (Ω-effect) and the generation of the poloidal magnetic field by currents associated with small-scale motions influenced by the Coriolis force acting on the toroidal field (α-effect) (Karak & Cameron 2016). According to Babcock-Leighton's solar cycle model, the cross-hemispheric coupling is also impacted by the regeneration of the poloidal magnetic field. This model illustrates how the poloidal magnetic field is reproduced and the variables that affect it (Charbonneau 2007). This model proposes that the decay of bipolar ARs exhibiting a systematic pattern of an inclination regarding East–West direction is required for the reproduction of the poloidal magnetic field (Babcock 1961; Leighton 1969). This inclination is caused by the Coriolis force acting on the flow that forms along the axis of the buoyantly rising magnetic loops that, when emerging in the photosphere, produce bipolar sunspot pairs. The Babcock-Leighton mechanism has the outstanding feature of being seen working on the solar surface (Wang & Sheeley 1991). Hence, pursuing solar dynamo modelling within this paradigm is only natural (Wang & Sheeley 1991; Durney 1995; Dikpati & Charbonneau 1999). In the context of Babcock-Leighton model, Charbonneau (2007) proposed that TLs could also be needed to build a stable cross-hemispheric coupling. The TL as a large-scale structure is influenced by many factors on the Sun. Therefore, the statistical study of the TL can be an aid to dynamo model theory.

Fárník et al. (1999) examined several TLs using the SXT data from Yohkoh and found that the length variation of these TLs could be due to differential rotation. Pevtsov (2000) studied 87 TL systems and analysed the foot-point distance, rotation rate, and helicity of the magnetic field. Through statistical analysis of 356 TLs from 1991 to 2001, Chen, Bao & Zhang (2006); Chen, Lundstedt & Zhang (2010) studied the relationship between TL and the solar cycle, and the twist value of TLs is related to flare flux. They also proposed that TLs preferentially connect preceding polarity magnetic field. However, due to the limited amount of data, only the descending period of Solar Cycle 22 and the ascending period of Solar Cycle 23 were studied. In order to confirm whether the statistical result is valid for other solar cycles, further research is needed.

The Hinode satellite (Kosugi et al. 2007) was launched in 2006, and the XRT telescope (Golub et al. 2007) on board has been observing the sun for more than ten years. Hinode/XRT has been collecting data from the Sun in soft X-ray light since 2006, which offers the possibility to further investigate TLs from a statistical point of view. In Section 2, we describe the source and reduction method of the data. In Section 3, we examine the properties of TLs, the relationship between the distance of the TL foot-point and time, the relationship between TLs and the number of sunspots, and the tilt angle and

asymmetry in latitude. The conclusion and discussion can be found in Section 4.

2 OBSERVATIONS AND DATA REDUCTION

In this paper, we use longitudinal magnetogram data from the Helioseismic and Magnetic Imager (HMI) (Scherrer et al. 2012) on the Solar Dynamics Observatory (SDO) and the Michelson Doppler Imager (MDI) (Scherrer et al. 1995) on the Solar and Heliospheric Observatory (SOHO). HMI (Centeno et al. 2014) is a filtergram-type instrument that observes (with a camera) Stokes *I*, *Q*, *U*, and *V* at six wavelength positions across the Fe I 6173 Å spectral line for the entire solar disc with 16 million pixels (4096×4096 CCD) every 45 s. (MDI) measures line-of-sight motion (Dopplergrams), magnetic field (magnetogram), and brightness images across the entire disc with a resolution of 4 arcsec or a smaller area of the solar disc with higher resolution (1.2 arcsec).

The Hinode XRT consists of the X-ray and visible light optics, the focal plane mechanisms (filters and shutter), and the $2K \times 2K$ CCD camera. At the same time, there are many filters that were made of different materials, e.g. Al-Mesh, Al-Poly. The different filters react differently to temperature. In this study, the Hinode/XRT data set from December 2006 to December 2020 is used, which includes the end of Solar Cycle 23, the whole Solar Cycle 24, and the beginning of Solar Cycle 25. We used the images, which were observed by Hinode XRT to identify the TLs. Then we used the HMI or MDI longitudinal magnetograms over the entire disc to derive magnetic information about the TLs.

We present below an example to describe how the data are selected and processed. First, we selected the image that revealed the clearest TL from the daily Hinode X-ray images of the entire Sun, such as Figs 1a and c. Then we downloaded the longitudinal magnetograms of the entire disc for the corresponding period, such as Figs 1b and d. Figs 1a and b show that the TL is called PTL, which formed by the preceding polarity connection of the ARs in the Northern and Southern hemispheres. As shown in Figs 1c and d, this type TL is called FTL, which formed by the following polarity connection of the ARs in the Northern and Southern hemispheres. We observed the image to determine whether TL belongs to PTL or FTL, and the magnetic field region where the TL foot-points are located.

Because the foot-points of TL are mainly distributed in the moderately strong field around the AR, there are also instances in which these loops are rooted in extremely weak or very strong fields, with values <30 G and several hundred G (Fárník, Karlický & Švestka 2001). There is also a situation where the foot-point of TL is located in the inactive region. Foot-points of the TLs cannot be located strictly at a single point.

Fig. 1d shows the full disc longitudinal magnetogram on 2016 February 6. We choose the magnetic polarity and surrounding area, where the foot-point of FTL is located. Concurrently, we used the white square frame to represent the range. We first filter out pixels that do not belong to this polarity. Then we weighted the magnetic field intensity of each point within the selected range to obtain the magnetic activity centre, which we define as the foot-point. For foot-points in the inactive region, we also use the same method to select the range that the foot-point contains as much as possible, and then obtain the foot-point position. Next, we converted the image coordinates of the foot-point position into Carrington latitude and longitude coordinates. Finally, we used two Carrington coordinate points to determine the distance between the foot-points in the Carrington coordinate system.
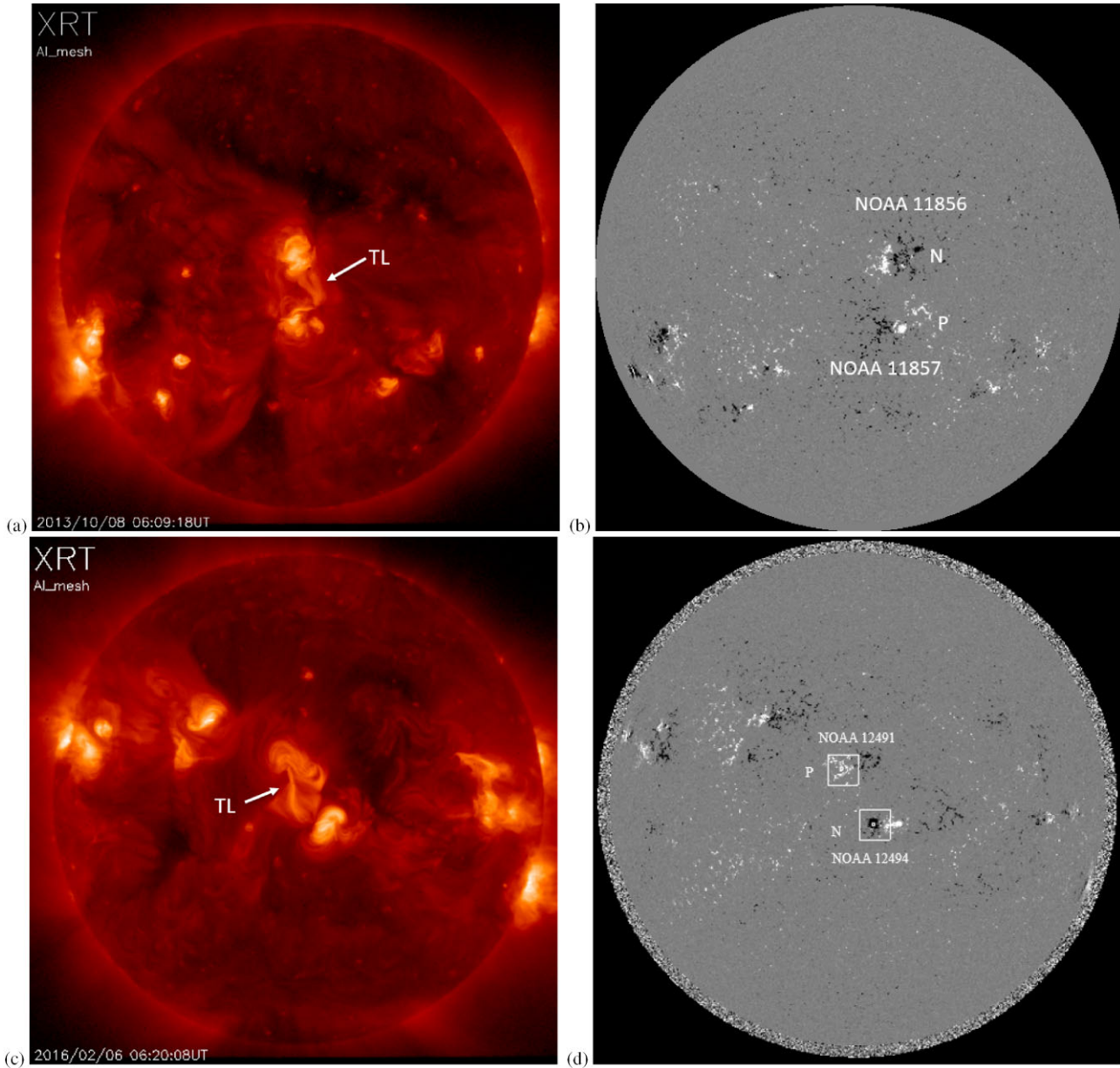
Figure 1. Images (a) and (c) are the soft X-ray images of the Hinode satellite. Images (b) and (d) are the magnetic field images of the HMI data. 'TL' is trans-equatorial loop, 'P' is positive magnetic polarity, 'N' is negative magnetic polarity. The white box represents the selected area.

3 PROPERTIES OF TRANS-EQUATORIAL LOOPS

The statistical characteristics of the TL from December 2006 to December 2020 are described in this section. The classification methods are discussed in the first part. In the second part, the relationship between foot-point distance and time is discussed. In the third and fourth parts, respectively, the tilt angle and asymmetry in latitude are discussed.

3.1 Classification

There are two classification approaches for TL. One is based on Pevtsov (2000)'s research. Using the X-ray shape, he describes a single loop or multiple loops connecting two regions in opposite

hemispheres as the 'connection' type, including sheared ('S type') or unsheared ('U type'). He also described the classical X-type and Y-type magnetic reconnection as the ' reconnection' type. The other classification is based on the magnetic polarity position of the TL foot-points. This study is based on the magnetic polarity position of the TL foot-points. As shown in the appendix, we counted 160 TLs and tabulated their main features: their observation date, the longitude, and latitude coordinates of the foot-points of the TLs in Carrington, the foot-point distance in degree and in solar radius units.

Due to the tilt of the ARs (Joy's law), the preceding magnetic polarity is typically closer to the solar equator than the following magnetic polarity. Joy's law was first observed by Hale et al. (1919). Joy's law describes the average magnetic field tilt of ARs with a leading magnetic polarity typically located closer to the solar equator than the following one. The opposite magnetic field in the Northern

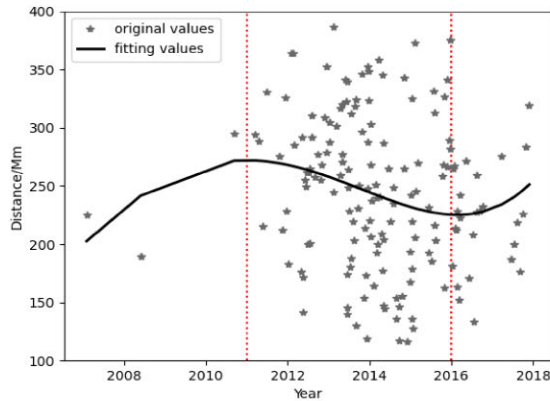**Table 1.** Statistics on the TL by foot-point classification.

Category	Number	Fraction (per cent)
PTL	118	74
FTL	42	26

and Southern hemispheres of the Sun, the polarity of the preceding magnetic field in the ARs of the Northern hemisphere is opposite to that in the ARs of the Southern hemisphere. This preferential orientation of ARs suggests that TLs are expected to be formed between the leading polarities of two ARs (located in different hemispheres). These TLs are called PTLs. However, in some cases, TLs are formed between the following polarities, which are called FTLs. Table 1 shows that the number of PTLs is 118, and the number of FTLs is 42. We found that there were 32 FTLs where the magnetic field of the following polarity was closer to the equator than that of the preceding polarity. These cases are not in accordance with Joy's law and belong to the anti-Hale type (Li 2018). They account for 76 per cent of the FTLs.
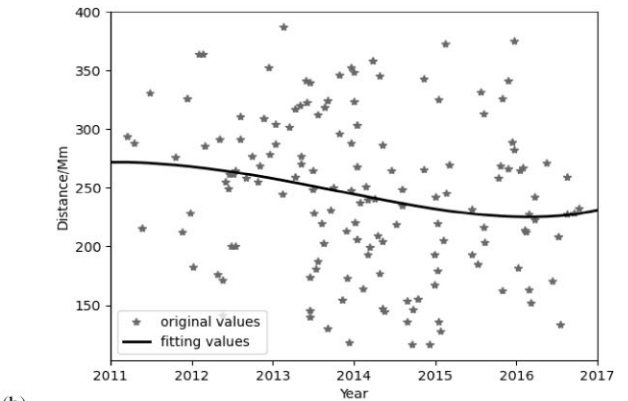
3.2 The relationship between the foot-point distance and the solar cycle

According to our research, a total of 1870 numbered ARs (data based on the Active Region Summary published by NOAA/USAF) were counted on the solar surface between December 2006 and December 2020. During this period, ARs associated with TL accounted for 12 per cent of the total. The maximum distance between TL foot-points is $31.9°$ (this corresponds to TL No. 39 in the Appendix), and the average value is $20°$.

Fig. 2 shows the change in the foot-point distance of TLs and the solar cycle from 2006 to 2020. To show the global trend of the foot-point distance in Fig. 2a, a polynomial adjustment was made to the data, which is shown by a solid line. Moreover, the period from December 2008 to December 2019 falls within Solar Cycle 24, so we can make a complete observation of Solar Cycle 24. The solar activity in Solar Cycle 24 is weaker than in Solar Cycles 22 and 23 (Charbonneau 2020). Chen et al. (2006) observed that there were 148 TL during the falling period of the Solar Cycle 22 and 208 TL during the rising period of Solar Cycle 23. There were 92 TL during the rising period and 66 TL during the falling period in Solar Cycle 24. Through comparison, we found that the rising period of the Solar
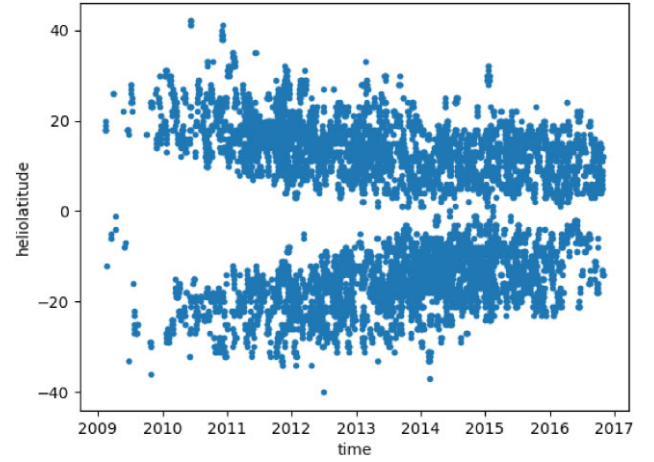

Figure 3. Latitude distribution map of sunspots from December 2008 to October 2016.

Cycle 24 was 116 TL less than the rising period of Solar Cycle 23, and the falling period of the Solar Cycle 24 was 82 TL less than the falling period of Solar Cycle 22.

The red-dashed lines in Fig. 2a delineate the statistical data from 2011 to 2016; they account for 84 per cent of the total data. For the further analysis in Fig. 2b, only the data from this period are used. Fig. 2b shows that the overall trend is declined, which corresponds to the change rule of the sunspot butterfly diagram of sunspots in Fig. 3.

Fig. 4 shows the change in the smoothed monthly mean sunspot and monthly TL counts from 2008 to 2018. The vertical red-dashed line in Fig. 4 is when solar activity reaches its maximum in Solar Cycle 24. The statistical analysis shows that 88 per cent of TLs occurred near the solar maximum (2014 ± 2), indicating that most TLs occurred around the solar maximum, which is similar to the distributions of near-ground events. For example, the interaction between relativistic solar protons and the Earth's atmosphere leads to an atmospheric cascade, thereby enhancing the intensity of cosmic rays observed by ground neutron monitors (Le & Liu 2020). Similarly, It's also includes strong solar proton events (Le et al. 2021b) and large geomagnetic storms (Le et al. 2021a) in the solar cycle.

(a)   (b)

Figure 2. Panel (a) shows the foot-point distance about TL at different times. The solid line is the result of polynomial fitting. The red-dotted lines indicates the selected year period for panel (b). The fitted polynomial is: $y_1 = a_1 \cdot t^4 + b_1 \cdot t^3 + c_1 \cdot t^2 + d_1 \cdot t + e_1 a_1 = 1.5 \times 10^{-4}, b_1 = -6.2 \times 10^{-1}, c_1 = -4.3 \times 10^{-1}, d_1 = 2.5 \times 10^6, e_1 = -2.5 \times 10^9$.
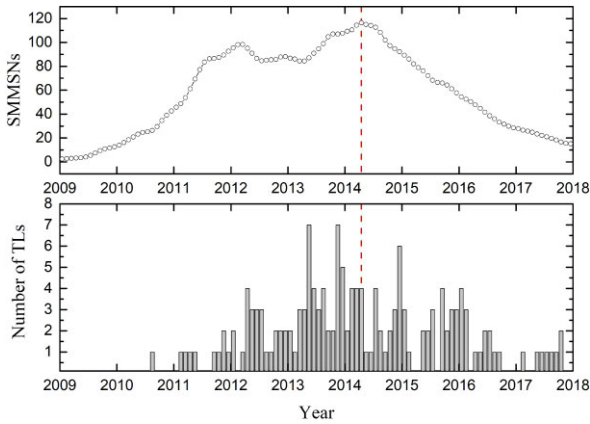
Figure 4. Solar cycle distribution of TLs from 2008 to 2018. The top and lower pannels are the smoothed monthly mean sunspot numbers (SMMSNs) and the monthly number of TLs, respectively. The vertical red-dashed line indicates the time when SMMSs reaches their maximum.

Table 2. The ratio of the number of ARs connected TL to the number of sunspots in different latitude ranges.

Latitude range	Number of sunspots	Number of TL	Ratio (per cent)
$20° \sim 30°$	679	1	0.2
$10° \sim 20°$	3135	61	2.0
$0° \sim 10°$	1440	93	6.5
$-10° \sim 0°$	917	86	9.4
$-20° \sim -10°$	2904	58	2.0
$-30° \sim -20°$	1101	1	0.1

From Fig. 4, it can be seen that the frequency of occurrence of TLs is somewhat related to the number of sunspots. When solar activity is high, the number of sunspots is also high and the number of TLs is correspondingly high.

It is well known that the behaviour about the equatorward drift of average sunspot latitudes is in accordance with Sporer's law (Ivanov & Miletsky 2014), which means that sunspots are formed at the beginning of the solar cycle at high latitudes and later on they are progressively formed closer to the equator (Hathaway et al. 2003). Table 2 shows, for the period from 2009 to 2016, the number of sunspot locations and the number of ARs connecting the TLs, as well as their ratios at different latitudes. Neglecting the difference between north and south, the results imply that the closer an AR is to the equator, the easier it is for AR to form a TL.

3.3 Tilt angle

The tilt angle is the angle between the equator and the TL. To calculate the tangent of the tilt angle, the differences between the latitude and longitude of the TL foot-points are used. If the northern foot-point is west of the southern foot-point, the tilt angle is defined as an acute angle between the solar equator and the segment joining the TL foot-points. If the northern foot-point is east of the southern foot-point, the tilt angle is defined as an obtuse angle. In order to clearly identify the tendency of the tilt angle to occur, we used the method of the Von Mises distribution as in (Fisher 1995). The Von Mises distribution is a continuous probability distribution, similar to the Gaussian distribution but adapted to parameters defined in a finite range, like the TL tilt here, with a range from 0 to 180°.

Fig. 5a shows the distribution of TL numbers at different angles of TL tilts. The red-dotted line in the figure represents the fitting result of the von Mises distribution, and the black-dotted line represents the average value of the distribution, which is around 90°. Fig. 5b shows the mean values of the tilt in function of time together with the corresponding standard deviations. In most cases, the annual mean values of the tilt angles are concentrated around 90°. At the same time, we also looked at the change in the tilt angle of the TLs during the ascent and descent phases of the solar cycle (Figs 6a and b). December 2008 to April 2014 was the rising period of the Solar Cycle 24, while May 2014 to December 2019 was the falling period of the Solar Cycle 24. The results show that the TLs' tilt angle is comparable for the rising and falling of the solar cycle.

3.4 Asymmetry in latitude

Latitude asymmetry is defined as the latitude of a TL's north foot-point minus the absolute value of the latitude value of its south. If the latitude of the northern base point is greater than that of the southern base point, the result is positive, otherwise it is negative.

The overall average of the latitudinal asymmetry is close to 0°, indicating that the TLs are nearly symmetrical in latitude. The distribution of TL asymmetry is shown in Fig. 7a. We used a Gaussian fitting for the distribution, as shown with the red-dotted line in the figure, and the black-dashed lines represent the number of cases. We found that the corresponding position of the highest point of the fitted image is around 0°. Fig. 7b shows the mean of latitude differences in different years. The annual average of the latitude difference is also 0°, indicating that the latitude asymmetry of the TLs does not change with the rising or falling of the solar cycle (Figs 8a and b).

4 CONCLUSION AND DISCUSSION

In this study, Hinode XRT data from December 2006 to December 2020 were used to obtain data for 160 TLs, mainly focusing on Solar Cycle 24, and statistical analyses were used to obtain certain observational characteristics of the TLs. The results are as follows:

(i) We have found that 74 per cent of the 160 TLs connected by ARs are PTLs. Meanwhile, 66 per cent of the 356 TLs counted by Chen et al. (2006) from 1991 to 2001 are PTLs. This indicates that TLs are formed preferentially between the preceding magnetic polarities of ARs, and this preference is independent of the solar cycle. In addition, we found that the number of TLs in the rising period of Solar Cycle 24 is less than that in the rising period of Solar Cycle 23, and the number of TLs in the falling period of Solar Cycle 24 is less than that in the falling period of Solar Cycle 22. This result could be due to the weak solar activity during Solar Cycle 24 (Hathaway 2015).

(ii) There are 24 per cent FTLs in the 160 TLs. Among these FTLs, 76 per cent FTLs are not consistent with Joy's Law. This type of FTL is connected with the following magnetic polarity of the AR to form a TL, and the following magnetic polarity is closer to the equator. Therefore, this asymmetry supports the idea that TLs are formed between the magnetic fluxes of ARs with closer spatial separation.

(iii) ARs connected by TLs account for at least 12 per cent of all ARs. It turns out that the closer AR is to the equator, the easier it is to form a TL. The probability of forming a TL in the latitude range of 0° to 10° is about four times higher than that of forming a TL in the latitude range of 10° to 20°.

(iv) The monthly number of TLs has a strong correlation with the level of solar activity. TLs occur mainly in years of high solar
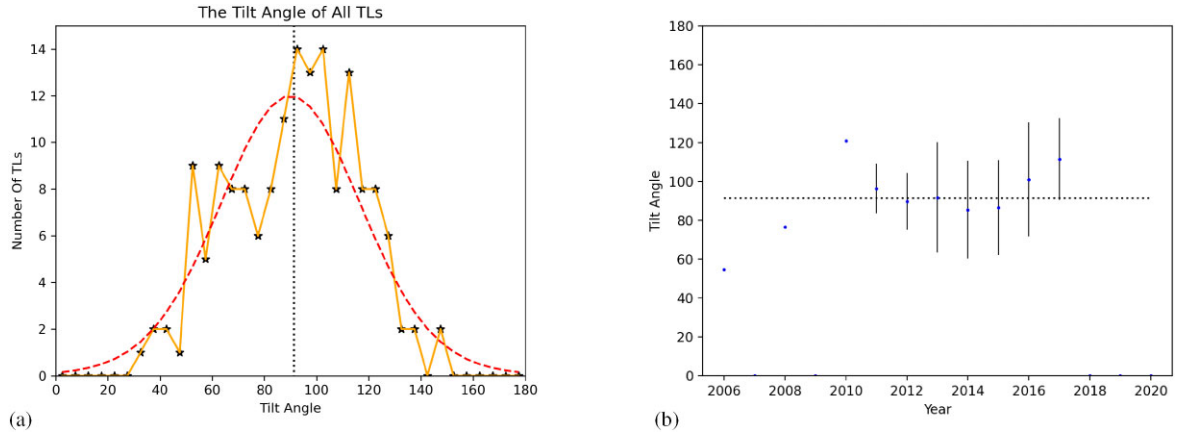
Figure 5. The tilt angle of the TLs. Diagram (a) is the data distribution of tilt angles. The red curve is the von Mises distribution fitting result. Diagram (b) is the tilt angle for different years. The blue dots show the annual mean of the tilt angle. Black lines over blue dots are error bars. The black dotted line represents the average value, which is 91.3.
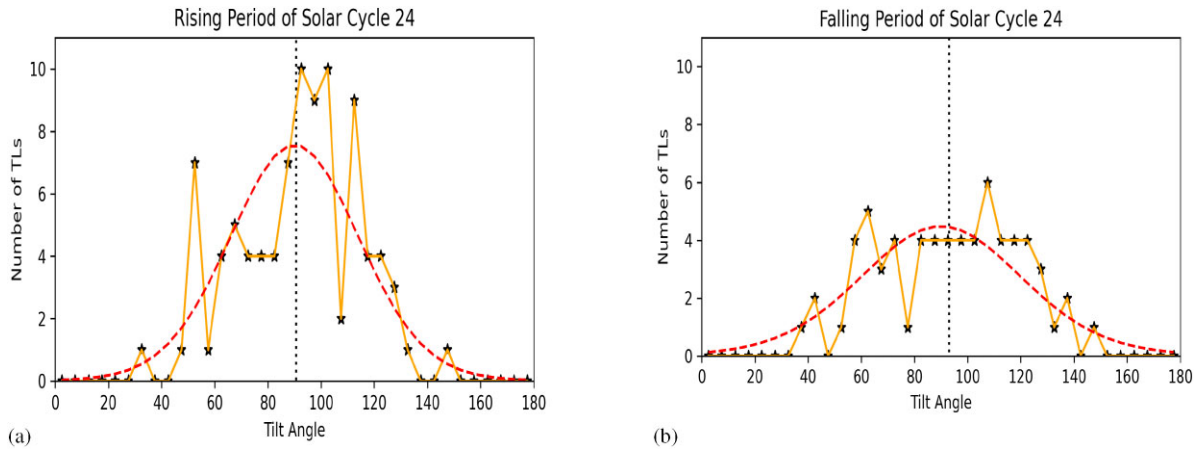
Figure 6. Diagram (a) shows the tilt angle distribution of the rising period of Solar Cycle 24, and Diagram (b) shows the tilt angle distribution of the falling period of Solar Cycle 24. Dashed lines represent number averages, where the value in the left figure is 90.7 and the value in the right figure is 93.
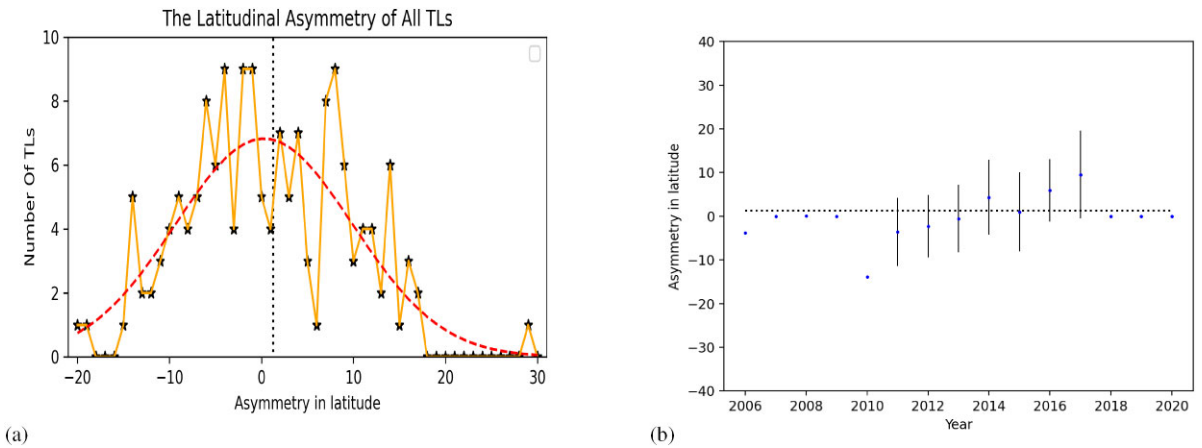
Figure 7. The latitudinal asymmetry of TLs. Diagram (a) shows the number distribution is asymmetric. The red-dotted line is the Gaussian distribution fitting result. Diagram (b) shows asymmetry in different years. The blue dots show the average latitude difference for each year. The black line above the blue dot is the error bar. The black dotted line represents the average value of the total latitude difference, which is 1.3.
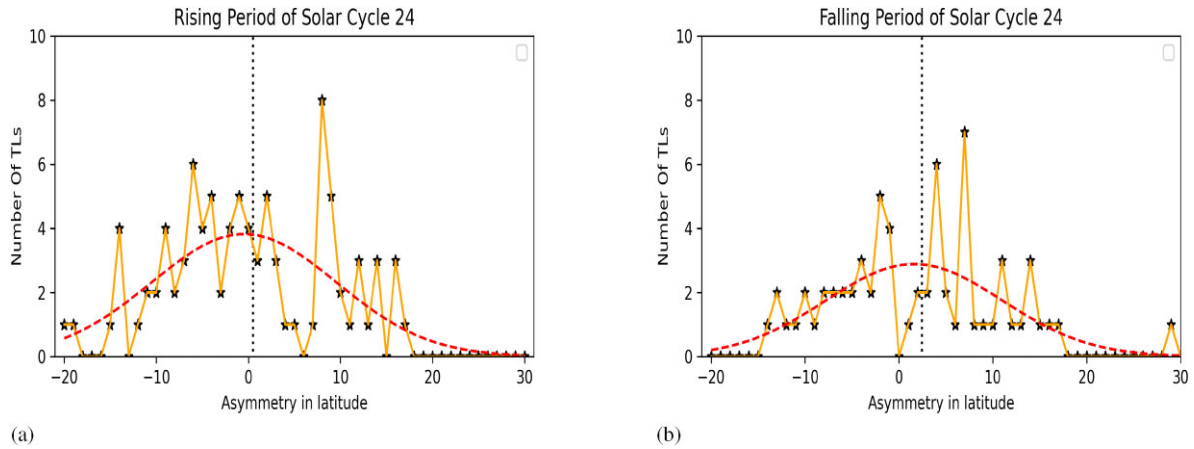
Figure 8. Diagram (a) shows the latitudinal asymmetry distribution of the rising period of Solar Cycle 24, and Diagram (b) shows the latitudinal asymmetry distribution of the falling period of Solar Cycle 24. Dashed lines represent number averages, where the value in the left figure is 0.5 and the value in the right figure is 2.4.

activity, and the number of sunspots is correlated to the number of TLs. We have found that 88 per cent of TLs occurred near the solar maximum (2014 ± 2). This variation in the number of TLs with the solar cycle is consistent with previous studies (e.g. Pevtsov 2000, 2004)). If TLs play a role in cross hemispheric coupling and the conversion of toroidal to poloidal fields, our results suggest that this conversion occurs throughout the solar cycle, with a peak around the maximum of the sunspot cycle.

(v) During Solar Cycle 24, the asymmetry of latitude and tilt angle has a weak correlation with the formation of TL. Next, as shown in Table 3, the percentage of PTLs in the ascent and descent periods is dominant, and the proportion of both is about 74 per cent.

The change of TL foot-point distance has a certain similarity with the change in the sunspot butterfly diagram. Under the influence of Sporer's law (Ivanov & Miletsky 2014), the average latitude of the centre of the sunspot drifts from high latitude to the equator. Meanwhile, influenced by differential rotation (Charbonneau 2020) and Hale's polarity law (Hale et al. 1919), the bipolar ARs in the same hemisphere have the same preceding magnetic polarity, while the bipolar ARs in the opposite hemisphere have the opposite trend of preceding polarity. AR is also influenced by Joy's law, the magnetic field of the preceding polarity is closer to the equator, and the magnetic field of the succeeding polarity is farther from the equator. Moreover, magnetic field of the preceding polarity is typically stronger and exists for a longer time than the magnetic field of the following polarity. The preceding polarity region has a stronger magnetic field, and a stronger magnetic field does not necessarily imply more dissipation since this strong field is also more coherent (more monolithic), so with less evolution. Moreover, chromospheric evaporation is caused by thermal conduction from the hot loop (Veronig & Brown 2004). Therefore, it is easier to see the magnetic reconnection of the preceding polarity magnetic field forming a TL.

The properties of TLs follow the properties of ARs. A preference for their formation between fields of leading polarity can be explained by the tilt angles of ARs (Joy's law), the shortening of their length during the solar cycle is the result of the average latitude of ARs drifting towards the equator (Sporer's law). Comparison with previous studies suggests that the total number of TLs depends on the amplitude of the solar cycle (total number of ARs in each cycle). The

Table 3. TL in Solar Cycle 24.

Period	Category	Number	Fraction (per cent)
2008.12–2014.04 (rising)	PTL	69	75
2008.12–2014.04 (rising)	FTL	23	25
2014.05–2019.12 (down)	PTL	49	74
2014.05–2019.12 (down)	FTL	17	26

fact that a significant fraction of ARs (35–40 per cent, Pevtsov 2000, 2004)) have trans-equatorial connections suggests that TLs play an important role in establishing magnetic connectivity between the Northern and Southern hemispheres.

However, Table 2 indicates that the number of TLs formed by AR in Solar Cycle 24 is much smaller than the number of TLs formed by AR in the previous solar cycle. Solar cycle 24 is far less strong than Solar Cycles 22 and 23 (Hathaway 2015), which are relatively strong and have many sunspots. In Solar Cycle 24, solar activity is weak and the number of sunspots is small. Therefore, the number of TLs is also low.

DATA AVAILABILITY

Data are available in a repository and can be accessed using a unique identifier other than a DOI. The data underlying this article are available in Joint Science Operations Center (JSOC), at http://jsoc.stanford.edu/How_toget_data.html. Permission to reproduce any third party material in your paper should have been obtained prior to acceptance. If your paper contains figures or text that require permission to reproduce, please confirm that you have obtained all relevant permissions and that the correct permission text has been used as required by the copyright holders.

REFERENCES

Babcock H. W., 1961, ApJ, 133, 572

Balasubramaniam K. S., Pevtsov A. A., Neidig D. F., Cliver E. W., Thompson B. J., Young C. A., Martin S. F., Kiplinger A., 2005, ApJ, 630, 1160

Centeno R., Schou J., Hayashi K., Norton A., Hoeksema J. T., Liu Y., Leka K. D., Barnes G., 2014, Sol. Phys., 289, 3531

Charbonneau P., 2007, Adv. Space Res., 40, 899

Charbonneau P., 2020, Living Rev. Sol. Phys., 17, 4

Chase R. C., Krieger A. S., Svestka Z., Vaiana G. S., 1976, in Proc. Open Meetings of Working Groups on Phys. Sciences and Symp. and Workshop on Results from Coordinated Upper Atmosphere Measurement Programs, Space research XVI. Akademie-Verlag GmbH, Berlin, p. 917

Chen J., Bao S., Zhang H., 2006, Sol. Phys., 235, 281

Chen J., Lundstedt H., Zhang H., 2010, Adv. Space Res., 45, 537

Chen J., Pevtsov A. A., Su J., Erdélyi R., Deng Y., Yang S., Song Y., 2020, Sol. Phys., 295, 59

Delannée C., 2000, ApJ, 545, 512

Dikpati M., Charbonneau P., 1999, ApJ, 518, 508

Durney B. R., 1995, Sol. Phys., 160, 213

Fárník F., Karlický M., Švestka Z., 1999, Sol. Phys., 187, 33

Fárník F., Karlický M., Švestka Z., 2001, Sol. Phys., 202, 81

Fisher N. I., 1995, Statistical Analysis of Circular Data. Cambridge University Press, Cambridge

Ghosh A., Tripathi D., 2020, A&A, 640, A3

Golub L. et al., 2007, Sol. Phys., 243, 63

Hale G. E., Ellerman F., Nicholson S. B., Joy A. H., 1919, ApJ, 49, 153

Hathaway D. H., 2015, Living Rev. Sol. Phys., 12, 4

Hathaway D. H., Nandy D., Wilson R. M., Reichmann E. J., 2003, ApJ, 589, 665

Ivanov V. G., Miletsky E. V., 2014, Geomag. Aeron., 54, 907

Kano R., Tsuneta S., 1995, ApJ, 454, 934

Karak B. B., Cameron R., 2016, ApJ, 832, 94

Khan J. I., Hudson H. S., 2000, Geophys. Res. Lett., 27, 1083

Kosugi T. et al., 2007, Sol. Phys., 243, 3

Le G.-M., Liu G.-A., 2020, Sol. Phys., 295, 35

Le G.-M., Zhao M.-X., Zhang W.-T., Liu G.-A., 2021a, Sol. Phys., 296, 187

Le G.-M., Zhao M.-X., Qi-Li, Liu G.-A., Mao T., Xu P.-G., 2021b, MNRAS, 502, 2043

Leighton R. B., 1969, ApJ, 156, 1

Li J., 2018, ApJ, 867, 89

Long D. M., Valori G., Pérez-Suárez D., Morton R. J., Vásquez A. M., 2017, A&A, 603, A101

Pevtsov A. A., 2000, ApJ, 531, 553

Pevtsov A. A., 2004, in Stepanov A. V., Benevolenskaya E. E., Kosovichev A. G. eds, IAU Symp. Vol. 223, Multi-Wavelength Investigations of Solar Activity. Cambridge University Press, Cambridge, p. 521

Scherrer P. H. et al., 1995, Sol. Phys., 162, 129

Scherrer P. H. et al., 2012, Sol. Phys., 275, 207

Svestka Z., Krieger A. S., Chase R. C., Howard R., 1977, Sol. Phys., 52, 69

Tsuneta S., 1996, ApJ, 456, L63

Veronig A. M., Brown J. C., 2004, ApJ, 603, L117

Wang Y. M., Sheeley N. R. J., 1991, ApJ, 375, 761

APPENDIX A: DATA OF TLS

Table A1. This table lists the relevant information of the 160 TLs, including TL occurrence time, TL number, foot-point polarity, foot-point carrington coordinates, foot-point distance in degrees, and in solar radius (R) units. The NOAA AR is set to 0 when the foot-point area has no AR number. 'N' represents the Northern hemisphere. 'S' represents the Southern hemisphere.

Number	Date	NOAA AR (N)	Polarity (N)	Longitude (N)	Latitude (N)	NOAA AR (S)	Polarity (S)	Longitude (S)	Latitude (S)	(°)	Distance
1	2006.12.29	0	+	125.8	5.7	10931	−	115.1	− 9.5	18.6	0.323 R
2	2008.04.27	0	−	103.9	7.6	0	+	100.3	− 7.6	15.6	0.27 R
3	2010.08.09	11093	−	32.4	3.5	11095	+	44.9	− 17.4	24.3	0.419 R
4	2011.02.14	0	+	270.7	10.5	11158	−	280.6	− 11.7	24.2	0.417 R
5	2011.03.13	0	−	292.8	12.8	11171	+	297.5	− 10.5	23.7	0.406 R
6	2011.04.18	11191	−	230.3	10.6	0	+	229.4	− 7.1	17.8	0.306 R
7	2011.05.23	0	−	168.6	15.9	11216	+	174.2	− 10.7	27.2	0.462 R
8	2011.09.18	11292	−	237.7	1.8	11299	+	238.3	− 20.9	22.7	0.383 R
9	2011.10.16	11319	−	211.0	3.7	11316	+	209.0	− 13.7	17.5	0.301 R
10	2011.11.08	11339	−	313.1	12.4	11338	+	323.6	− 12.3	26.8	0.461 R
11	2011.11.22	11353	−	113.9	5.0	11354	+	116.6	− 13.6	18.8	0.323 R
12	2011.12.04	11362	−	372.9	5.0	0	+	369.4	− 9.6	15.0	0.26 R
13	2012.01.01	11390	−	48.0	11.1	11388	+	35.7	− 16.3	29.9	0.512 R
14	2012.01.18	0	−	183.3	11.1	11399	+	171.0	− 16.3	29.9	0.512 R
15	2012.01.30	0	+	31.1	16.0	0	−	34.2	− 7.3	23.5	0.401 R
16	2012.03.26	0	+	68.7	9.1	11438	−	66.8	− 5.3	14.5	0.251 R
17	2012.04.05	11451	−	347.5	18.6	0	+	347.4	− 5.4	24.0	0.406 R
18	2012.04.16	0	+	198.9	6.8	11454	−	200.9	− 4.7	11.7	0.203 R
19	2012.04.16	0	−	203.1	7.8	11454	+	205.6	− 6.1	14.1	0.244 R
20	2012.04.30	11467	−	18.2	9.7	11469	+	22.0	− 11.0	21.0	0.361 R
21	2012.05.11	11476	−	270.1	10.6	0	+	270.1	− 9.9	20.5	0.353 R
22	2012.05.18	11484	−	170.2	15.6	11481	+	173.6	− 5.7	21.5	0.368 R
23	2012.05.27	11408	−	63.2	10.1	0	+	65.4	− 6.2	16.5	0.284 R
24	2012.06.06	11498	−	330.5	8.8	11494	+	332.4	− 12.6	21.5	0.369 R
25	2012.06.15	11506	−	218.9	7.9	11505	+	221.3	− 8.4	16.5	0.285 R
26	2012.06.15	11506	+	210.1	8.3	11504	−	215.1	− 12.9	21.8	0.375 R
27	2012.07.03	11513	−	26.7	11.2	11515	+	19.9	− 13.5	25.6	0.437 R
28	2012.07.03	11516	−	16.8	9.0	11515	+	17.4	− 15.0	24.0	0.409 R
29	2012.07.29	11528	−	35.9	8.2	11529	+	30.4	− 12.3	21.2	0.365 R
30	2012.08.25	11548	−	92.2	8.5	11552	+	82.9	− 12.4	22.8	0.393 R
31	2012.09.24	11575	−	95.1	1.1	11576	+	95.2	− 19.9	21.0	0.355 R
32	2012.10.01	11580	+	362.6	9.9	11579	−	370.6	− 10.7	22.1	0.381 R
33	2012.10.21	11593	−	103.6	5.7	11594	+	99.3	− 19.3	25.4	0.43 R
34	2012.11.11	0	−	234.5	9.4	11608	+	237.8	− 19.5	29.0	0.489 R
35	2012.11.16	11615	−	165.4	5.4	11613	+	175.5	− 15.3	23.0	0.396 R
36	2012.12.12	11629	−	231.9	9.4	0	+	220.3	− 12.9	25.1	0.433 R
37	2012.12.12	0	−	206.5	7.8	0	+	207.7	− 15.8	23.7	0.403 R
38	2013.01.13	11654	−	197.5	11.9	11657	+	202.7	− 7.6	20.2	0.347 R
39	2013.01.16	11654	+	177.2	14.0	11658	−	151.2	− 4.7	31.9	0.559 R
40	2013.02.11	0	+	233.9	16.1	0	−	218.4	− 3.5	24.8	0.431 R
41	2013.03.09	0	+	247.6	17.0	11689	−	244.0	− 8.9	26.1	0.443 R
42	2013.03.09	0	−	269.3	14.5	11683	+	278.1	− 5.0	21.4	0.368 R
43	2013.03.30	11704	−	350.4	18.2	11707	+	332.5	− 1.5	26.4	0.459 R
44	2013.04.04	11708	−	323.3	14.3	11711	+	312.8	− 5.4	22.3	0.385 R
45	2013.04.04	11708	−	323.4	14.3	11710	+	336.2	− 4.7	22.8	0.395 R
46	2013.04.26	11727	−	43.4	18.8	0	+	36.1	− 8.4	28.1	0.477 R
47	2013.05.01	11731	−	369.8	6.9	11732	+	347.5	− 7.6	26.6	0.465 R
48	2013.05.15	11744	−	184.6	7.1	0	+	182.5	− 4.2	11.5	0.2 R
49	2013.05.15	11745	+	149.4	12.3	11746	−	151.9	− 15.6	28.0	0.473 R
50	2013.05.15	11744	−	167.3	8.3	11747	+	170.6	− 5.6	14.3	0.248 R
51	2013.05.16	11744	+	175.5	7.1	11750	−	177.8	− 4.7	12.0	0.209 R
52	2013.05.26	11753	−	44.5	6.7	11754	+	50.7	− 12.9	20.5	0.353 R
53	2013.05.26	11755	−	32.1	8.6	11756	+	39.8	− 11.8	21.8	0.375 R
54	2013.06.02	0	−	361.8	12.0	11757	+	372.4	− 3.6	18.8	0.327 R
55	2013.06.10	0	−	239.0	5.5	0	+	244.7	− 8.2	14.9	0.238 R
56	2013.06.19	11776	−	127.5	9.9	11769	+	130.5	− 15.7	25.7	0.437 R
57	2013.06.19	11773	−	112.5	3.4	11770	+	119.7	− 10.3	15.4	0.268 R
58	2013.07.08	0	−	289.7	4.6	11788	+	278.9	− 9.9	18.1	0.315 R
59	2013.07.16	11792	−	157.0	1.6	11791	+	165.7	− 12.7	16.7	0.29 R
60	2013.07.20	11793	−	109.4	14.8	11795	+	124.8	− 6.5	26.2	0.455 R

Table A1 – *continued*

Number	Date	NOAA AR (N)	Polarity (N)	Longitude (N)	Latitude (N)	NOAA AR (S)	Polarity (S)	Longitude (S)	Latitude (S)	(°)	Distance
61	2013.08.03	11809	−	308.6	7.7	0	+	318.0	− 17.3	26.7	0.456 R
62	2013.08.03	11811	+	329.7	2.1	0	−	331.9	− 8.4	10.7	0.186 R
63	2013.08.16	0	+	163.1	8.6	11818	−	171.4	− 8.5	19.0	0.33 R
64	2013.08.30	11834	−	340.8	7.1	11835	+	332.8	− 11.9	20.6	0.356 R
65	2013.09.25	11850	+	35.4	3.7	11851	−	22.0	− 16.8	24.4	0.422 R
66	2013.09.25	11850	−	44.6	4.4	11846	+	62.9	− 17.6	28.5	0.495 R
67	2013.10.08	11856	−	222.8	3.8	11857	+	222.6	− 8.9	12.7	0.22 R
68	2013.10.23	11875	+	17.7	3.0	11877	−	6.7	− 10.7	17.6	0.306 R
69	2013.11.01	11883	−	308.2	2.7	11884	+	308.4	− 11.5	14.3	0.246 R
70	2013.11.08	0	−	217.7	4.0	11890	+	221.1	− 5.2	9.8	0.17 R
71	2013.11.16	11899	−	111.5	7.7	11895	+	113.1	− 15.9	23.7	0.404 R
72	2013.11.18	11899	+	78.4	2.9	11897	−	99.0	− 17.8	29.0	0.506 R
73	2013.11.18	11899	−	84.8	3.6	0	+	71.7	− 12.2	20.4	0.356 R
74	2013.11.28	11905	−	306.8	15.3	11907	+	319.8	− 8.0	26.6	0.459 R
75	2013.11.28	11905	+	301.9	15.2	11906	−	301.8	− 13.4	28.7	0.484 R
76	2013.12.05	0	+	254.8	8.1	11916	−	250.3	− 9.5	18.1	0.313 R
77	2013.12.12	12922	+	194.3	9.4	0	−	180.5	− 7.9	22.1	0.384 R
78	2013.12.12	12923	−	151.9	11.9	12917	+	158.3	− 12.2	25.0	0.427 R
79	2013.12.15	11921	−	123.1	6.9	11918	+	134.0	− 6.2	17.0	0.296 R
80	2013.12.24	0	−	− 6.0	9.4	11931	+	− 5.4	− 10.1	19.5	0.336 R
81	2014.01.09	11946	−	216.2	12.3	11944	+	215.7	− 1.2	13.5	0.233 R
82	2014.01.22	11957	+	42.0	15.9	11955	−	35.9	− 3.8	20.6	0.354 R
83	2014.02.03	11968	+	282.0	16.2	0	−	273.1	− 1.5	19.8	0.341 R
84	2014.02.03	11968	−	291.1	15.0	11967	+	292.8	− 0.8	15.9	0.273 R
85	2014.02.11	11973	+	185.3	12.6	11974	−	175.4	− 0.6	16.4	0.286 R
86	2014.02.22	11986	−	1.7	16.8	11982	+	26.3	− 0.1	29.5	0.518 R
87	2014.03.02	11989	−	311.1	13.7	11995	+	302.6	− 4.2	19.8	0.342 R
88	2014.03.15	0	−	130.3	15.8	12004	+	129.7	− 1.4	17.2	0.294 R
89	2014.03.24	12013	−	14.1	20.2	12014	+	− 2.7	− 3.0	28.4	0.491 R
90	2014.03.24	0	+	− 11.0	11.7	12014	−	− 11.4	− 2.9	14.6	0.252 R
91	2014.04.06	12029	−	259.5	9.8	12026	+	255.3	− 1.6	12.1	0.211 R
92	2014.04.06	12030	+	231.7	17.1	0	−	227.5	− 6.2	23.6	0.402 R
93	2014.04.06	12030	−	237.7	16.2	12028	+	244.0	0.5	16.8	0.289 R
94	2014.04.15	12034	−	121.6	10.4	12037	+	122.0	− 1.6	11.9	0.207 R
95	2014.05.15	12063	−	97.7	11.7	12061	+	108.5	− 7.2	21.8	0.378 R
96	2014.06.07	12081	−	231.4	9.9	12080	+	224.3	− 6.7	18.0	0.313 R
97	2014.07.04	12102	−	275.4	8.5	12104	+	267.5	− 9.1	19.3	0.335 R
98	2014.07.04	12106	+	253.0	9.6	12108	−	240.2	− 6.4	20.5	0.357 R
99	2014.07.27	12121	+	315.1	3.4	12126	−	316.9	− 7.7	11.2	0.195 R
100	2014.07.27	12121	−	320.9	3.6	12123	+	321.9	− 9.0	12.6	0.219 R
101	2014.08.19	12142	−	76.1	2.8	12143	+	78.0	− 6.6	9.6	0.167 R
102	2014.08.23	12148	−	17.8	2.3	12147	+	19.6	− 9.6	12.1	0.209 R
103	2014.09.14	0	−	135.3	4.1	12164	+	138.6	− 8.2	12.8	0.222 R
104	2014.10.08	12183	−	192.4	5.7	12184	+	177.6	− 18.4	28.2	0.486 R
105	2014.10.08	0	+	155.3	7.5	12185	−	153.9	− 14.3	21.8	0.374 R
106	2014.11.04	0	−	238.6	3.8	12201	+	234.0	− 4.5	9.6	0.167 R
107	2014.11.26	12219	+	301.6	5.2	12220	−	302.3	− 10.7	15.9	0.275 R
108	2014.11.26	12219	−	306.1	4.7	12216	+	314.1	− 6.6	13.8	0.24 R
109	2014.12.02	12221	−	266.2	5.7	12222	+	266.2	− 14.2	19.9	0.341 R
110	2014.12.12	12234	−	136.3	5.6	12230	+	140.5	− 8.5	14.7	0.256 R
111	2014.12.12	12232	−	116.1	11.5	12235	+	105.7	− 3.4	18.1	0.314 R
112	2014.12.16	12239	−	74.1	15.0	12233	+	93.5	− 3.7	26.8	0.468 R
113	2014.12.16	12238	+	67.2	5.0	12237	−	65.6	− 6.0	11.2	0.194 R
114	2014.12.23	0	−	347.4	7.2	12244	+	339.4	0.3	10.5	0.184 R
115	2015.01.08	12257	−	152.4	10.4	12255	+	150.3	− 6.3	16.9	0.292 R
116	2015.01.13	12258	−	97.8	18.3	12259	+	88.1	− 10.9	30.7	0.521 R
117	2015.01.20	12264	+	343.6	16.6	12266	−	356.1	0.5	20.2	0.351 R
118	2015.02.03	12277	−	221.1	12.1	0	+	210.4	− 7.5	22.2	0.385 R
119	2015.05.13	12345	−	96.0	16.3	12340	+	90.9	− 2.1	19.1	0.327 R
120	2015.05.13	12343	+	79.1	13.1	12340	−	86.3	− 1.1	15.9	0.275 R
121	2015.06.07	12360	−	171.3	14.5	12358	+	177.0	0.4	15.2	0.263 R
122	2015.06.22	12371	+	327.8	11.8	0	−	305.7	− 4.5	27.3	0.478 R
123	2015.07.05	12373	−	206.2	11.2	12375	+	194.5	− 11.8	25.8	0.444 R

Table A1 – *continued*

Number	Date	NOAA AR (N)	Polarity (N)	Longitude (N)	Latitude (N)	NOAA AR (S)	Polarity (S)	Longitude (S)	Latitude (S)	(°)	Distance
124	2015.07.05	12376	+	187.9	9.6	12375	−	192.4	− 7.6	17.8	0.307 R
125	2015.07.08	12381	−	147.8	9.7	12383	+	154.7	− 5.6	16.7	0.29 R
126	2015.09.11	12411	−	127.9	9.9	12414	+	124.8	− 11.1	21.3	0.365 R
127	2015.09.18	12419	−	8.3	6.4	12418	+	10.9	− 15.6	22.1	0.378 R
128	2015.09.26	12420	+	266.7	7.4	12422	−	266.9	− 19.4	26.9	0.453 R
129	2015.09.26	12420	−	275.8	4.6	12425	+	282.0	− 7.2	13.4	0.233 R
130	2015.10.22	12436	−	276.3	4.6	12435	+	284.7	− 15.7	21.9	0.377 R
131	2015.10.22	12436	+	275.4	6.6	12437	−	265.6	− 19.7	28.1	0.477 R
132	2015.11.10	12448	+	83.8	4.7	12449	−	66.7	− 11.9	23.8	0.415 R
133	2015.11.18	12454	+	331.4	8.8	0	−	317.5	− 18.9	30.9	0.528 R
134	2015.11.18	12454	−	341.4	9.9	0	+	340.5	− 13.3	23.2	0.397 R
135	2015.12.09	12462	−	105.4	10.4	12463	+	102.0	− 4.2	15.0	0.259 R
136	2015.12.16	0	−	21.4	13.8	12468	+	19.7	− 7.9	21.8	0.373 R
137	2015.12.28	12472	+	212.9	7.8	12473	−	216.4	− 13.9	22.0	0.377 R
138	2016.01.08	12477	−	85.9	16.3	0	+	80.3	− 0.4	17.6	0.302 R
139	2016.01.12	12480	−	28.3	9.5	0	+	33.8	− 7.0	17.5	0.302 R
140	2016.01.24	12488	−	227.3	10.0	12486	+	241.4	− 2.4	18.8	0.328 R
141	2016.01.24	0	−	247.6	9.6	12486	+	241.4	− 2.4	13.5	0.234 R
142	2016.02.06	12491	+	102.5	9.5	12494	−	108.7	− 1.5	12.5	0.218 R
143	2016.02.20	12501	+	275.6	11.5	0	−	281.3	− 5.9	18.3	0.317 R
144	2016.02.20	12503	−	298.2	6.5	0	+	287.1	− 10.1	19.9	0.346 R
145	2016.04.13	12529	−	13.6	16.3	0	+	21.0	− 4.8	22.3	0.383 R
146	2016.05.10	12542	−	58.7	15.2	12543	+	62.6	1.7	14.0	0.241 R
147	2016.06.06	0	−	113.8	13.8	0	+	118.1	− 2.8	17.1	0.295 R
148	2016.06.16	0	−	327.7	7.5	12553	+	331.4	− 2.9	11.0	0.191 R
149	2016.07.14	12564	−	− 4.8	8.0	12562	+	8.2	− 5.5	18.7	0.327 R
150	2016.07.14	12563	−	11.2	15.9	12562	+	8.6	− 5.3	21.3	0.365 R
151	2016.08.14	12574	−	5.1	2.9	12576	+	− 5.6	− 12.6	18.8	0.327 R
152	2016.09.06	12585	−	114.6	4.5	12584	+	130.8	− 5.8	19.1	0.335 R
153	2017.02.24	12638	+	164.9	24.3	12637	−	177.3	5.0	22.7	0.388 R
154	2017.05.20	12656	−	236.6	14.7	12658	+	231.3	0.2	15.4	0.266 R
155	2017.06.16	0	−	291.6	14.7	0	+	291.0	− 1.7	16.5	0.283 R
156	2017.07.13	12666	−	341.1	11.2	12665	+	351.4	− 3.6	18.0	0.313 R
157	2017.08.08	0	−	46.1	11.0	12670	+	54.2	− 1.1	14.5	0.253 R
158	2017.09.04	12674	−	95.0	7.7	12673	+	102.3	− 9.5	18.6	0.322 R
159	2017.10.01	12683	−	78.5	9.0	12682	+	91.4	− 10.4	23.3	0.405 R
160	2017.10.27	12686	−	81.6	13.1	12685	+	97.2	− 8.2	26.3	0.456 R

This paper has been typeset from a TEX/LATEX file prepared by the author.